Article

UDC 621.35:621.382.3:546.77

https://doi.org/10.31489/2025PH3/16-30

Received: 29.05.2025
Accepted: 26.06.2025

S. Adaikhan, K.Zh. Bekmyrza, A.A. Baratova✉, A.M. Kabyshev, P. Rajagopal, N.K. Aidarbekov, K.K. Kuterbekov, M.M. Kubenova, M.D. Kuanysh

L.N. Gumilyov Eurasian National University, Astana, Kazakhstan

Development and Characterization of Nanostructured Ni–ScSZ Composite Anodes for Solid Oxide Fuel Cells

A thorough investigation was carried out on nickel-based anode composites with scandia-stabilized zirconia (Ni/ScSZ), fabricated using ceramic processing techniques from powders with varying particle sizes. The study emphasizes the role of initial component morphology and their ratios on sintering behavior, electrical conductivity, and polarization resistance under solid oxide fuel cell (SOFC) operating conditions. Samples incorporating nano-, submicron-, and micron-sized particles were comparatively analyzed to determine the most favorable parameters for constructing a percolative conductive network and reducing polarization losses. Experimental data obtained through dilatometry, electrical measurements, and electrochemical impedance spectroscopy confirmed that the use of nanoscale constituents leads to the formation of a dense and uniform microstructure with well-distributed porosity. Such features enhance both thermal stability and electrochemical performance. The findings highlight the potential of Ni/ScSZ-based materials as a viable alternative to conventional Ni/YSZ anodes, owing to their improved ionic conductivity and enhanced resistance to degradation, thus contributing to the advancement of more durable and efficient SOFC technologies.

Keywords: solid oxide fuel cell (SOFC), Ni/ScSZ composite anode, nanopowder dispersion, polarization resistance, triple-phase boundary, electrical conductivity, sintering kinetics, activation energy, impedance spectroscopy, fabrication method

✉*Corresponding author*: Baratova Aliya, aa.baratova@yandex.kz

Introduction

Solid oxide fuel cells (SOFCs) utilizing yttria-stabilized zirconia (YSZ) as the electrolyte represent one of the most promising technologies for converting chemical energy of fuels into electricity, owing to their high efficiency and environmental benefits. Currently, nickel-YSZ cermet (Ni/YSZ) is widely employed as the anode material in such systems due to its excellent electrocatalytic activity in hydrogen and syngas oxidation reactions [1, 2]. However, the stable and efficient operation of SOFCs with this type of anode typically requires elevated temperatures (above 800 °C), which imposes limitations on the selection of compatible materials for other cell components and increases the demands on the thermal and chemical durability of the overall structure [3, 4].

To reduce the operating temperature and enhance the durability of anodes, intensive research is being conducted to improve their catalytic and transport properties. Key strategies include tailoring the microstructure of anode materials and replacing the conventional YSZ electrolyte with solid electrolytes exhibiting higher ionic conductivity [5, 6]. Among the most promising alternatives is scandia-stabilized zirconia (ScSZ), which demonstrates oxygen ion conductivity that is two to three times higher than that of YSZ. Incorporating ScSZ into the anode cermet enhances the electrochemical performance by extending the active triple-phase boundary and reducing the tendency for carbon deposition during the operation with hydrocarbon fuels [7, 8].

This issue is particularly critical for cermet-based anodes employing scandia-stabilized zirconia (ScSZ), which lacks intrinsic electronic conductivity. In such systems, the electrochemical performance strongly depends on the quality of the interface between the electronic and ionic phases. When the chemical composition is fixed, the functional characteristics of the anode can be significantly enhanced by introducing nanostructured components. These materials increase the density of active triple-phase boundaries, facilitate charge transfer, and reduce polarization losses. Another promising strategy involves engineered macrostruc-

turing of the electrode architecture to optimize gas diffusion pathways and ensure long-term stability under extended operation [9–13].

Accordingly, the objective of this study is to develop and characterize nanostructured Ni–ScSZ composite anodes and to evaluate how particle size and phase ratio influence the microstructure, electrical conductivity, polarization resistance, and sintering kinetics of anodes intended for solid oxide fuel cells (SOFCs). The findings aim to identify optimal processing conditions for fabricating high-performance anodes and constructing a model fuel cell with elevated specific power output.

Materials and methods

Initial powders

Initial powders of NiO and ScSZ with nano- and submicron-scale particle sizes were employed in this study, differing in both chemical nature and synthesis technique. Nanopowders of NiO (Ni-n) and ScSZ (ScSZ-n, containing 10.5 mol% Sc_2O_3) were synthesized by the methods of wire electrical explosion [14] and laser evaporation [15], respectively. These synthesis routes are known to produce materials with high surface reactivity and a dense population of electrochemically active sites.

As submicron materials, a commercial NiO powder from the Ural Chemical Reagents Plant (Ni-m) and thermally treated ScSZ-n powder were used. The ScSZ-n powder was calcined at 1000 °C for 4 hours and then manually ground to obtain submicron-sized ScSZ (ScSZ-m). These materials exhibited lower specific surface areas (2.7 and 8.4 m^2/g, respectively) and significantly larger particle sizes-up to 325 nm for Ni-m and 125 nm for ScSZ-m—suggesting pronounced aggregation and crystallite growth during the heat treatment process.

Table 1 summarizes the nomenclature and key physicochemical properties of the precursor powders used for the fabrication of the anode composites. The table includes chemical composition, specific surface area determined by the Brunauer–Emmett–Teller (BET) method (S_{BET}), equivalent particle diameter calculated from BET data (d_{BET}), and theoretical density (γ_{theor}). Analysis of these data reveals that the nanopowders Ni-n and ScSZ-n exhibit significantly higher surface areas (14.3 and 81.5 m^2/g, respectively) and smaller equivalent particle sizes (56 and 13 nm, respectively) compared to their submicron counterparts, Ni-m and ScSZ-m. These characteristics confirm their nanoscale nature, reflecting a high degree of dispersion and a developed surface morphology that favors enhanced phase interaction in the composite anodes. In contrast, the submicron powders show signs of particle agglomeration and growth, particularly in the case of Ni-m (d_{BET} = 325 nm), which may adversely affect mass transport and reduce the density of electrochemically active regions in the final electrode structure. Despite these morphological and textural differences, the theoretical density remains constant for powders of identical chemical composition, as it is an intrinsic property of the bulk material.

Table 1

Nomenclature and properties of the initial powders

Designation	Composition	α	β (fm^3)	γ_{rtheor}, $g/sm^3\gamma$
Ni-n	NiO	14.3	56	6.80
Ni-m	NiO	2.7	325	6.80
ScSZ-n	$Zr_{0.81}Sc_{0.19}O_{1.905}$	81.5	13	5.67
ScSZ-m	$Zr_{0.81}Sc_{0.19}O_{1.905}$	8.4	125	5.67

Figure 1 presents the morphology of the four powders studied, as observed using transmission electron microscopy (TEM) performed on a Jeol JEM-2100 instrument. Analysis of the micrographs in Figure 1 revealed that the ScSZ-n nanopowder (Fig. 1*a*) consists of uniformly distributed, near-spherical particles with a low degree of agglomeration. The particles appear well-dispersed, indicating the high efficiency of the laser evaporation technique employed in their synthesis.

In contrast, the ScSZ-m powder (Fig. 1*b*), obtained through calcination followed by mechanical grinding, exhibits irregularly shaped aggregates with a clumped morphology, indicating a strong tendency for particle agglomeration after thermal treatment.

The NiO nanopowder (Ni-n), shown in Figure 1*c*, consists of nearly spherical particles with minimal aggregation; the majority of the particles fall within the expected size range of 50–60 nm.

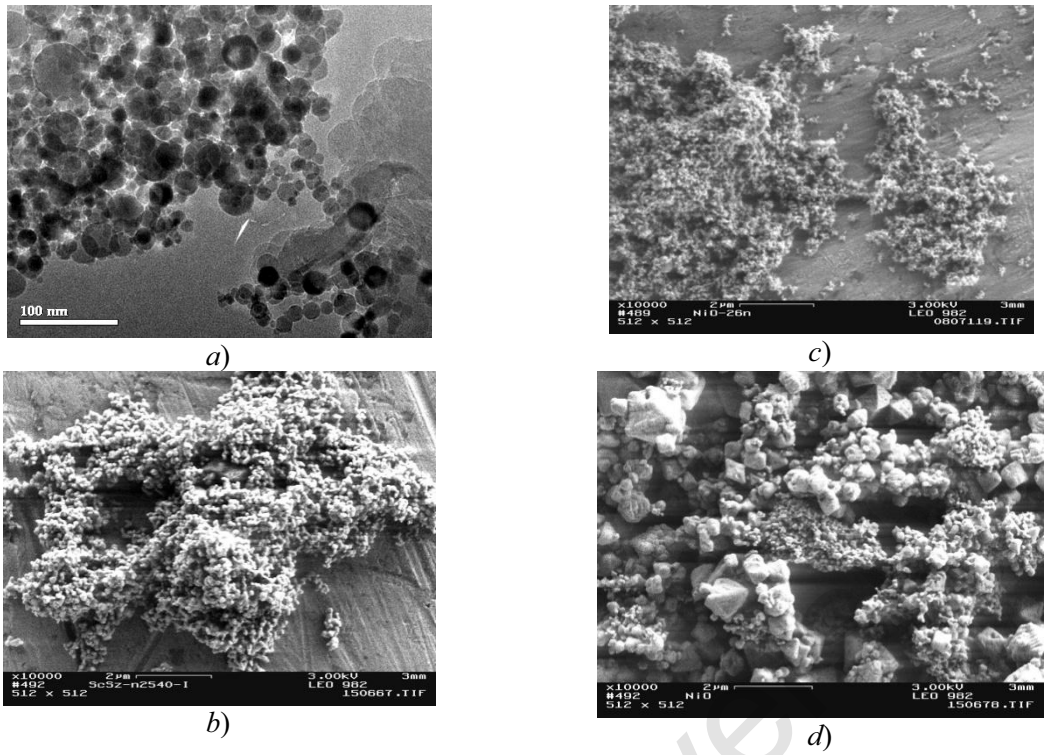

a) *c*)

b) *d*)

Figure 1. Microstructure of ScSZ and NiO powders with different particle sizes, obtained by transmission electron microscopy (Jeol JEM-2100): (*a*) ScSZ-n; (*b*) ScSZ-m; (*c*) Ni-n; (*d*) Ni-m

Meanwhile, the submicron NiO powder (Ni-m) presented in Figure 1*d* reveals a pronounced bimodal particle size distribution: along with fine fractions (~200 nm), large, well-faceted crystallites up to 1–1.5 μm are also observed. Such morphology may adversely affect the homogeneity and electrical conductivity of the resulting anode composites.

Sample preparation

Three types of samples were prepared from the synthesized composite powders for studying sintering kinetics, electrical conductivity, and polarization resistance. To investigate sintering behavior, disk-shaped specimens with a diameter of 8 mm and a thickness of approximately 2 mm were fabricated using magnetic impulse pressing, achieving a relative density of 0.65–0.68. The sintering measurements were conducted in air within a temperature range of 20–1500 °C using a Dil 402C dilatometer.

To measure electrical conductivity, the composite powders were statically pressed into rectangular bars measuring 3×2×30 mm, with a relative density of 0.65. The optimal mass and pressing pressure were selected to ensure sample reproducibility. The Ni-n/ScSZ-n and Ni-n/ScSZ-m composites were sintered at 1200 °C, while the Ni-m/ScSZ-m composition was sintered at 1400 °C, with a dwell time of 4 hours in each case. After sintering, platinum probes with a diameter of 0.2 mm were attached to the samples. The specimens were then reduced in a hydrogen atmosphere at 900 °C for 1 hour. Electrical measurements were carried out using the four-probe DC method in humidified hydrogen (3 % H_2O) in the temperature range of 700–900 °C in 50 °C increments using a Solartron SI-1260/1287 system. The density of the reduced samples was determined by hydrostatic weighing.

Polarization resistance of the anodes was measured using impedance spectroscopy on symmetrical cells with a solid-state ScSZ electrolyte in the form of a disk. The electrolyte was fabricated from a green tape composed of 87.2 wt.% ScSZ-n, 10 wt.% polyvinyl butyral (PVB), and 2.8 wt.% triethylene glycol dimethacrylate (TEGDMA). Circular disks with a diameter of 15 mm were cut from the tape, uniaxially pressed at 300 MPa, and sintered at 1250 °C for 4 hours. The resulting dense electrolyte pellets had a diameter of approximately 12 mm and a thickness of about 0.3 mm. Anode layers were applied by a painting technique using an ink composed of isopropanol, 82.1 wt.% Ni/ScSZ powder, 14 wt.% PVB, and 3.9 wt.% TEGDMA. The thickness of the deposited layers ranged from 20 to 30 μm. Firing of the anode layers was carried out in air at 1200 °C for Ni-n/ScSZ-n, 1250 °C for Ni-n/ScSZ-m, and 1300 °C for Ni-m/ScSZ-m composites, with a uniform dwell time of 4 hours. Prior to measurements, the electrodes were reduced in a

hydrogen atmosphere at 900 °C for 1 hour. Impedance measurements were performed in the frequency range from 0.1 Hz to 1 MHz, with an input signal amplitude of 10 mV, in the temperature range of 700–900 °C with 50 °C increments.

Results and discussion

Sintering kinetics

Figure 2 presents the temperature-dependent relative shrinkage curves for the initial powders and the composite materials derived from them.

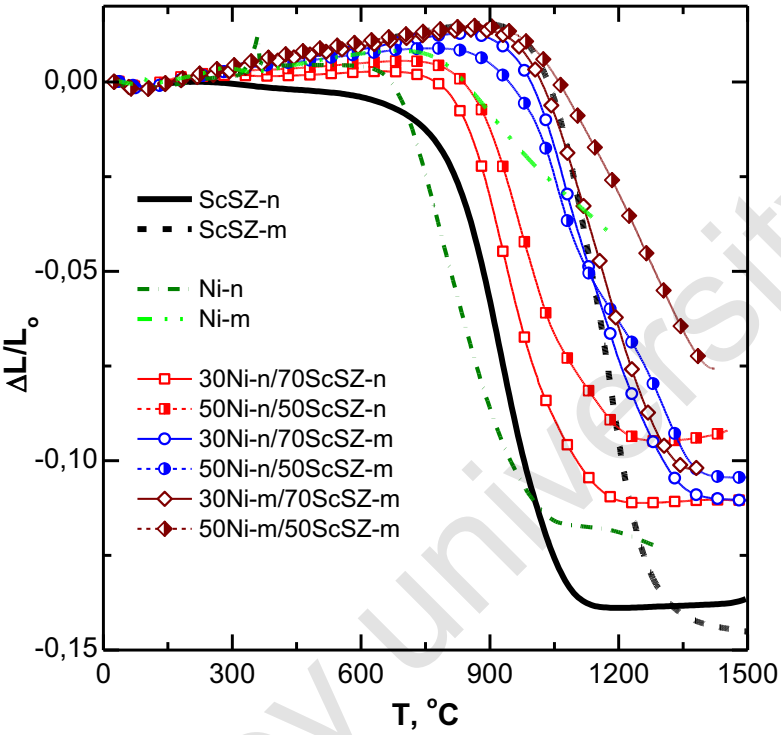

Figure 2. Linear shrinkage curves of compacted samples made from the initial powders and their corresponding composite materials

Analysis of the data reveals that samples prepared from nanoscale NiO (Ni-n) and ScSZ (ScSZ-n) powders complete the sintering process at temperatures below 1200 °C, with a divergence of no more than 2.5 % between their respective shrinkage curves. In contrast, samples formed from submicron powders (Ni-m and ScSZ-m) exhibit a shift in the onset of intensive shrinkage by 200–250 °C toward higher temperatures. Furthermore, the divergence between their shrinkage curves at 1200 °C reaches 5.4 %.

Composites incorporating the nanosized NiO component (Ni-n), specifically 30Ni-n/70ScSZ-n, 50Ni-n/50ScSZ-n, 30Ni-n/70ScSZ-m, and 50Ni-n/50ScSZ-m, exhibit a shift in the sintering temperature range to higher values—by approximately 50–80 °C-compared to their individual constituents. It was found that increasing the volume fraction of NiO in the composite leads to a higher sintering temperature and a reduction in total shrinkage. For Ni-n/ScSZ-n composites containing 30 and 50 vol.% Ni, the mismatch in shrinkage with the ScSZ-n electrolyte was approximately 3 % and 4.5 %, respectively. Similar trends were observed in the Ni-n/ScSZ-m and Ni-m/ScSZ-m systems, although the effect was less pronounced in the Ni-n/ScSZ-m series. This is likely attributed to the slower sintering kinetics of the coarser ScSZ-m powder, which plays a dominant role in the overall densification behavior of the composite.

Electrical conductivity of cermet composites

Figure 3 presents the dependence of electrical conductivity on the nickel volume fraction for three types of Ni/ScSZ anode composites measured at 900 °C. Analysis of these curves reveals several important insights into the nature of charge transport and the structural characteristics of the studied materials. According to the data presented in Figure 3, a sharp increase in electrical conductivity is observed when the nickel content exceeds 30 vol.%. This phenomenon is attributed to reaching the percolation threshold, beyond which a

continuous electron-conducting network formed by metallic nickel is established throughout the material. Below this threshold, conductivity is predominantly ionic in nature, governed solely by the solid electrolyte ScSZ.

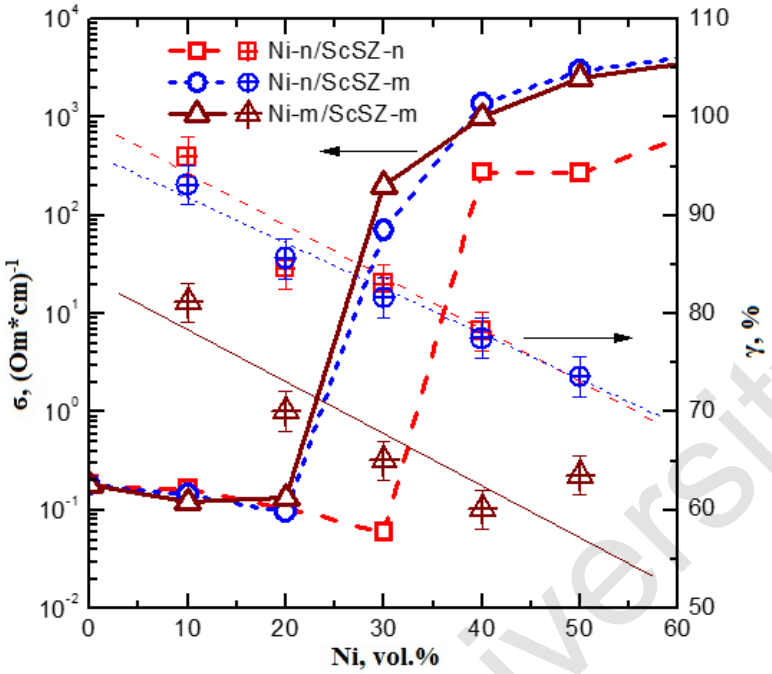

Figure 3. Electrical conductivity of three types of Ni/ScSZ anode composites at 900 °C as a function of nickel volume content (cross symbols indicate the relative density of the samples after reduction in hydrogen—right axis)

A comparative analysis of the three types of composites—Ni-n/ScSZ-n, Ni-n/ScSZ-m, and Ni-m/ScSZ-m-reveals distinct features in the transition from ionic to electronic conductivity (Fig. 3). In the Ni-n/ScSZ-n composite, this transition occurs more abruptly and is shifted toward higher nickel concentrations (~35 vol.%), which is likely due to the mismatch in particle sizes between the Ni-n nanoparticles (dBET = 56 nm) and the nano-sized ScSZ electrolyte (dBET = 13 nm). During composite preparation, the smaller ScSZ particles tend to envelop the larger Ni particles, thereby hindering the formation of continuous electronic pathways.

In the Ni-n/ScSZ-m composite, which incorporates nanostructured nickel (Ni-n) and submicron-sized electrolyte (ScSZ-m), the transition to electronic conductivity appears more gradual (Fig. 3). This behavior may be attributed to the lower surface area of ScSZ-m, which results in less extensive coverage of Ni particles and, consequently, an earlier formation of a continuous electronic network. Such morphological characteristics promote a more uniform distribution of nickel and improved interparticle contact, reflected in a steady increase in overall conductivity.

For the Ni-m/ScSZ-m composite, composed of submicron components, the conductivity increases more gradually, with the transition from ionic to electronic conduction occurring near 30 vol.% Ni. This behavior is attributed to the lower active surface area and coarser structure of the powders, which hinder the formation of continuous conductive pathways. Additionally, the increase in NiO content leads to a reduction in the sample density due to its reduction to metallic Ni—an effect associated with a significant volumetric expansion (~41 %) during the reduction process [16].

Figure 3 also presents the values of relative density after reduction (indicated by cross-marked symbols on the right axis). It can be observed that an increase in Ni content leads to a decrease in density due to increased porosity, which also affects the overall conductivity behavior.

Polarization resistance

Figure 4 displays the temperature-dependent electrical conductivity of various anode composites based on nanoscale nickel (Ni-n) and submicron electrolyte ScSZ-m. In part (*a*) of the figure, it is evident that the

conductivity of the 30Ni-n/70ScSZ-m and 40Ni-n/60ScSZ-m composites decreases with increasing temperature, indicating the predominance of metallic (electronic) conduction.

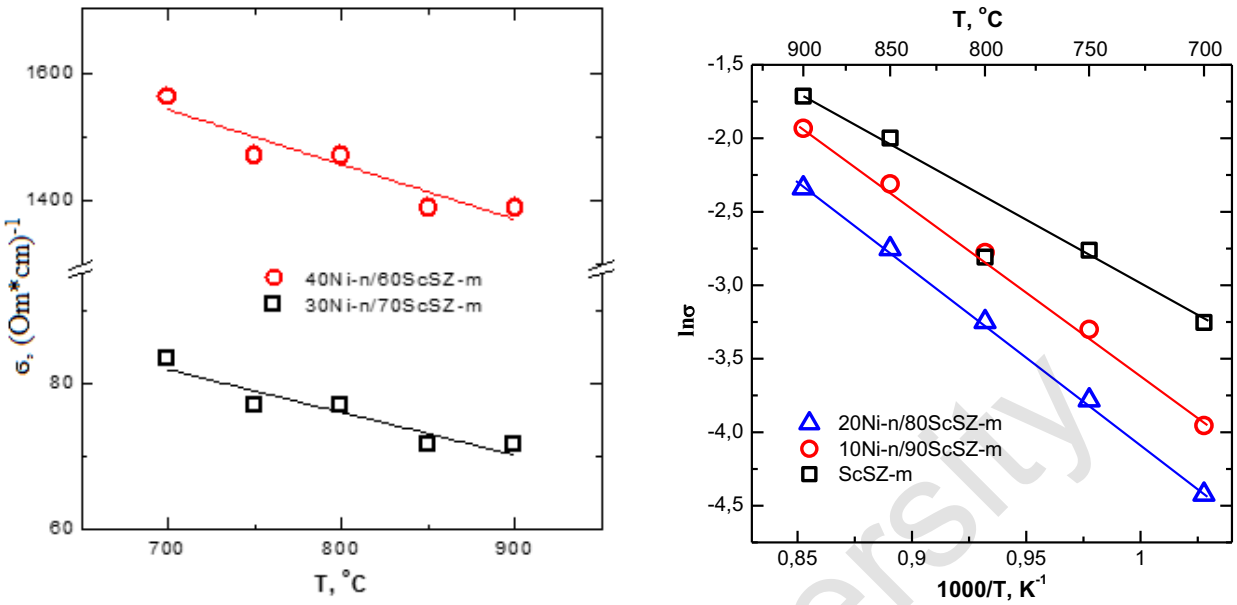

Figure 4. Temperature dependences of conductivity for composite mixtures: *a*) 40Ni-n/60ScSZ-m, 30Ni-n/70ScSZ-m, *b*) 20Ni-n/80ScSZ-m, 10Ni-n/90ScSZ-m, ScSZ-m

Such behavior is characteristic of composites containing more than 30 vol.% of nickel, where a continuous electronically conductive network is formed.

Part (*b*) of Figure 4 displays the conductivity behavior of compositions with lower nickel content — 10 and 20 vol.%. These composites exhibit an increase in conductivity with rising temperature, indicating an ionic conduction mechanism, which is characteristic of the ScSZ-based electrolyte matrix. The pure ScSZ composition, without any Ni addition, serves as a reference sample and shows the lowest conductivity values across the entire temperature range, further confirming its purely ionic conductivity nature.

The analysis of the impedance spectra presented in Figure 5 highlights the influence of the gas atmosphere on the impedance response of a symmetric cell featuring a 50Ni-n/50ScSZ-m anode composition at 900 °C. The impedance plots are shown in the complex plane format (Re(Z), –Im(Z)), with the real part of the impedance (Ohm) on the x-axis and the negative imaginary component (Ohm) on the y-axis, oriented downward—consistent with the standard representation of Nyquist plots.

Figure 5 presents three impedance spectra corresponding to different gas compositions: 100 %, 50 %, and 25 % hydrogen diluted with argon.

Each spectrum exhibits the shape of two overlapping semicircles, with each arc representing a distinct electrochemical process occurring at the anode. The high-frequency arc, located on the left side of the Nyquist plot, is associated with charge transfer across the electrode–electrolyte interface and is characterized by the resistance $R_{\eta-HF}$. In contrast, the low-frequency arc on the right side is attributed to diffusion and surface-related phenomena such as hydrogen adsorption, transport, and electrochemical conversion. This arc is described by the resistance $R_{\eta-LF}$.

The equivalent circuit shown in the inset of Figure 5 consists of a series resistance Rs (ohmic resistance) and two parallel RC elements (or constant phase elements, CPEs), representing the polarization resistances $R_{\eta\text{-}HF}$ and $R_{\eta\text{-}LF}$.

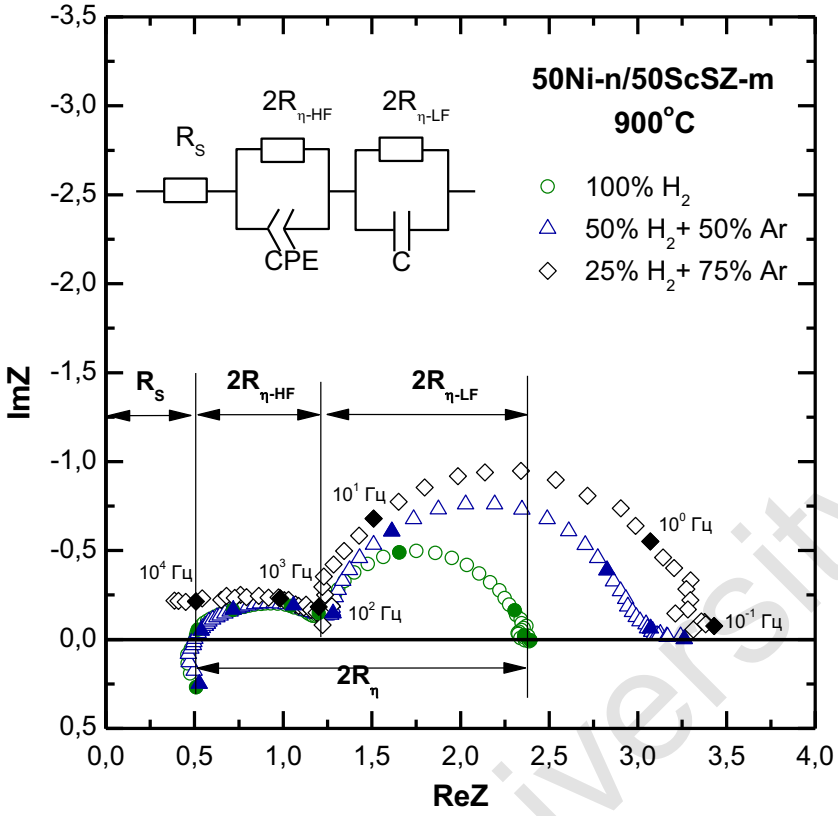

Figure 5. Impedance spectra of the 50Ni-n/50ScSZ-m electrode measured at 900 °C in hydrogen atmospheres of varying concentration (inset—equivalent circuit diagram)

The duplication of these resistances in the model stems from the symmetrical configuration of the cell, where identical anodes on both sides contribute equally to the overall impedance.

Analysis of the arc shapes and sizes indicates that as hydrogen concentration decreases, the most significant changes occur in the low-frequency region: the radius of the low-frequency arc ($R_{\eta\text{-LF}}$) increases markedly when transitioning from 100 % to 25 % H_2. This trend reflects a deterioration in surface activity and increased difficulty of hydrogen diffusion, particularly along the triple-phase boundary. Thus, lowering the hydrogen partial pressure reduces the efficiency of the anodic processes, as evidenced by the rise in polarization resistance. Meanwhile, the high-frequency component ($R_{\eta\text{-HF}}$), associated with charge transfer across the anode/electrolyte interface, remains virtually unchanged, indicating stable interfacial contact and minimal influence of gas composition on this mechanism [17].

Thus, the total polarization resistance of the anode ($R = R_{\eta-HF} + R_{\eta-LF}$) increases with decreasing hydrogen concentration, primarily due to the rise in $R_{\eta-LF}$. These findings confirm the high sensitivity of the 50Ni-n/50ScSZ-m composite to the composition of the reducing atmosphere and emphasize the critical role of gas environment control in the operation of SOFC anodes.

Figure 6 illustrates the temperature-dependent behavior of the total polarization resistance of Ni/ScSZ anode composites, as well as its high-frequency and low-frequency components.

Analysis of the data shows that the high-frequency contribution ($R_{\eta\text{-HF}}$) exhibits typical thermally activated behavior and follows an Arrhenius-type dependence. This indicates that charge transfer across the interface between the ionically and electronically conductive phases is an energetically driven process. The observed trend reflects temperature-sensitive kinetics and underscores the effectiveness of interfacial interactions near the triple-phase boundary.

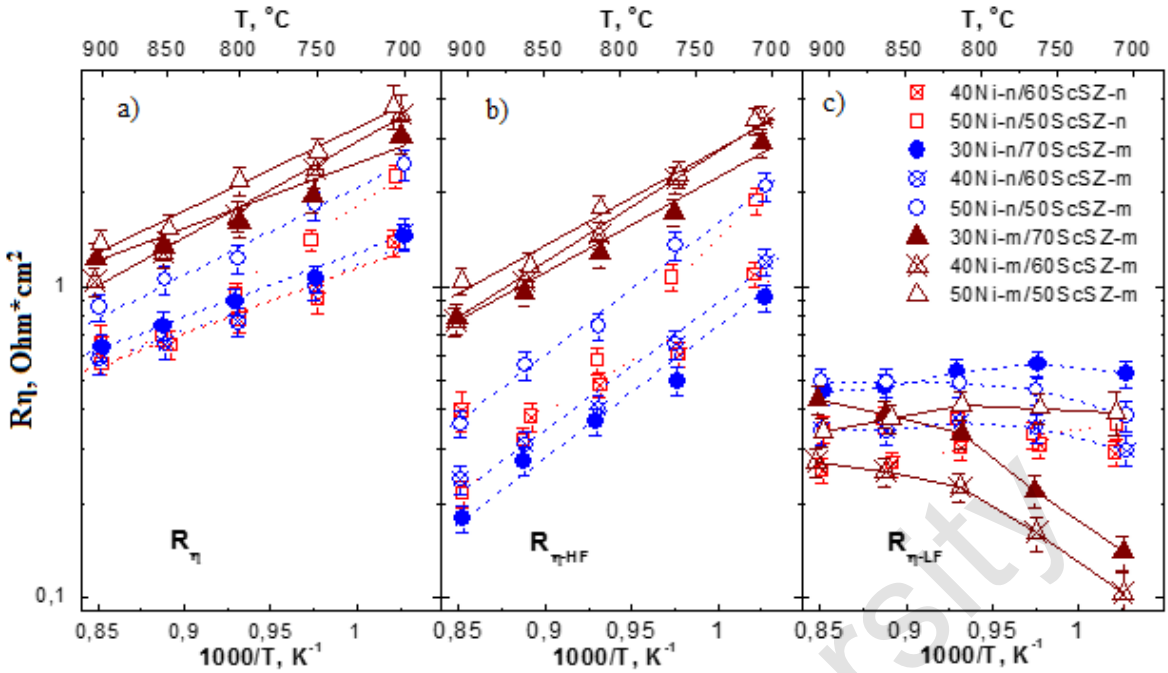

Figure 6. Temperature dependence of the polarization resistance of Ni/ScSZ composite anodes: (*a*) total polarization resistance as a function of temperature; (*b*) temperature dependence of the high-frequency component; (*c*) temperature dependence of the low-frequency component

Analysis of graph (*b*) in Figure 6, which illustrates the temperature dependence of the high-frequency component of polarization resistance ($R_{\eta\text{-HF}}$), clearly highlights the effect of particle size on charge transfer efficiency at the electrode–electrolyte interface. The lowest resistance values (ranging from 0.2 to 0.3 Ohm·cm^2 at 900 °C) were observed for the anode composed of nano-sized nickel and nano-structured electrolyte (50Ni-n/50ScSZ-n). The second-best performance was demonstrated by the anode based on nano-nickel and submicron electrolyte (50Ni-n/50ScSZ-m), which exhibited a slightly higher resistance in the range of 0.4–0.6 Ohm·cm^2. Despite the reduced dispersion of one phase, the composite based on nano-nickel and submicron electrolyte still maintains favorable electrochemical performance, underscoring the predominant role of the metallic component's dispersion. The highest $R_{\eta\text{-HF}}$ values (approximately 0.8–1.0 Ohm·cm^2) were observed for the anode entirely composed of submicron powders (50Ni-m/50ScSZ-m). This increased resistance is attributed to the less developed microstructure and the limited number of effective contacts between the conducting and ionic phases, resulting in a lower density of active triple-phase boundaries. All the presented curves follow an Arrhenius-type trend, confirming the thermally activated nature of the high-frequency process and its sensitivity to temperature. Part (*c*) of Figure 6 presents the temperature dependence of the low-frequency component of the polarization resistance ($R_{\eta\text{-LF}}$), which is primarily associated with surface and diffusion-related processes. Unlike the high-frequency contribution, the temperature dependence of $R_{\eta\text{-LF}}$ is relatively weak. The resistance values remain nearly constant, averaging around 0.3 ± 0.2 Ohm·cm^2. This indicates that mass transport and adsorption phenomena at the anode surface are not significantly influenced by temperature within the studied range. The similarity of $R_{\eta\text{-LF}}$ values across all anode types can be attributed to their comparable porosity (~55 ± 10 %), as confirmed by water absorption measurements.

Figure 7 presents SEM images of fracture cross-sections of symmetrical cells with an "electrode–electrolyte–electrode" architecture, incorporating different types of anodes: 50Ni-n/50ScSZ-n, 40Ni-n/60ScSZ-m, and 40Ni-m/60ScSZ-m.

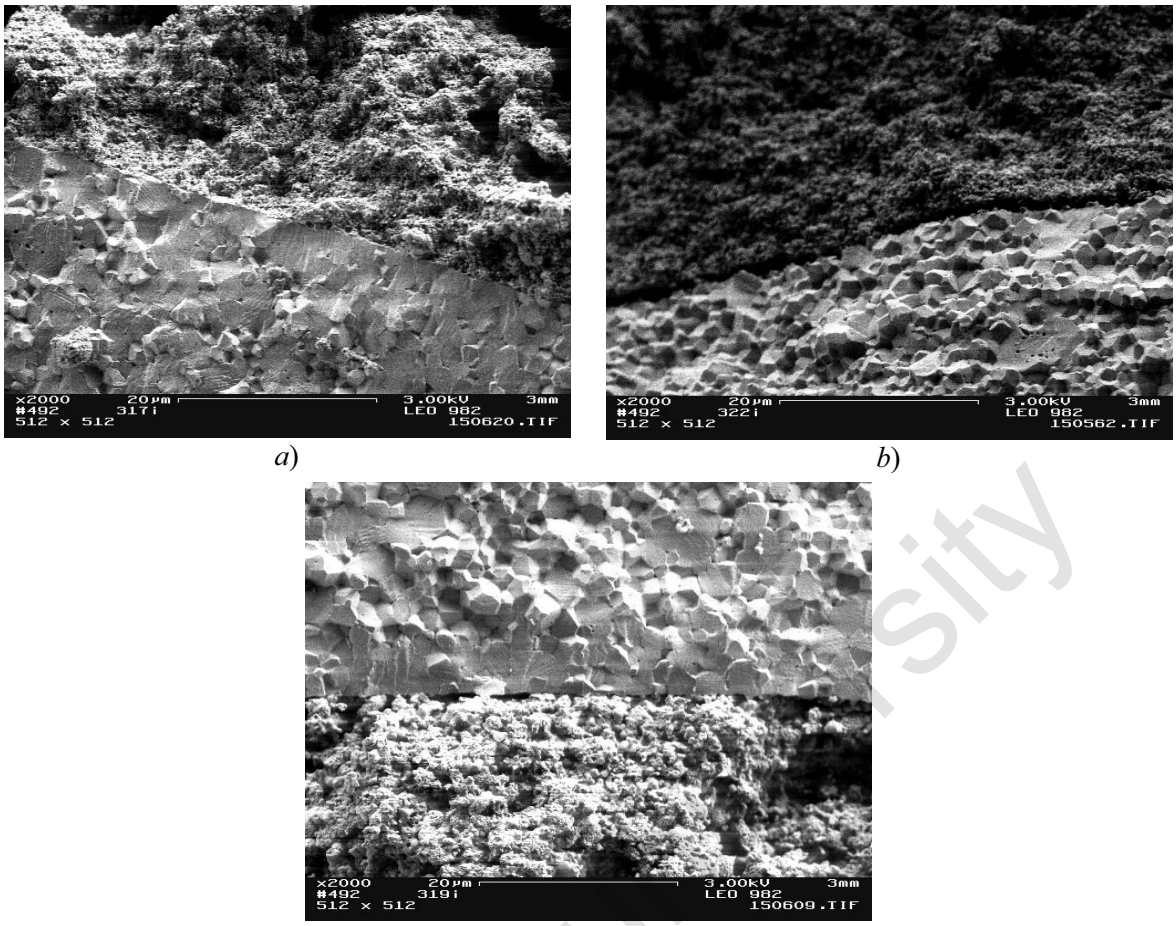

Figure 7. SEM images of fracture cross-sections of "electrode–electrolyte–electrode" structures with different types of electrodes: (*a*) electrode type—50Ni-n/50ScSZ-n; (*b*) electrode type—40Ni-n/60ScSZ-m; (*c*) electrode type—40Ni-m/60ScSZ-m

The analysis of these micrographs shows that, in all samples, the solid electrolyte layer is densely sintered and free of visible structural defects such as cracks or voids, indicating high sintering quality. The electrodes are firmly bonded to the electrolyte, with clearly defined interfaces and no signs of delamination or poor adhesion, confirming the mechanical integrity and suitability of the fabricated composite structures for high-temperature SOFC operation.

Furthermore, a strong visual cohesion between the electrode and electrolyte is evident, with no detectable separation or interface discontinuity—an essential criterion for maintaining long-term electrochemical stability under thermal cycling conditions. In all three cases, the porosity within the electrode layer appears uniformly distributed, with pore sizes predominantly in the submicron range. This morphology is beneficial for gas permeability and enhances the effective area of the triple-phase boundary, which is critical for efficient electrochemical reactions in SOFC anodes.

Additionally, the interface between the nickel-based anode and the electrolyte was examined using energy-dispersive spectroscopy (EDS), the results of which confirmed a homogeneous distribution of nickel within the near-surface region and the absence of diffusion zones depleted in conductive phases (Fig. 8). This effect was particularly evident in the anodes containing nanostructured nickel (50Ni-n/50ScSZ-n and 40Ni-n/60ScSZ-m), where the high dispersity of the metallic phase ensured closer phase contact and a higher density of conductive pathways.

Figure 8 presents the results of energy-dispersive spectroscopy (EDS) conducted at the electrode–electrolyte interface for symmetrical cells incorporating different types of anodes: 50Ni-n/50ScSZ-n, 40Ni-n/60ScSZ-m, and 40Ni-m/60ScSZ-m.

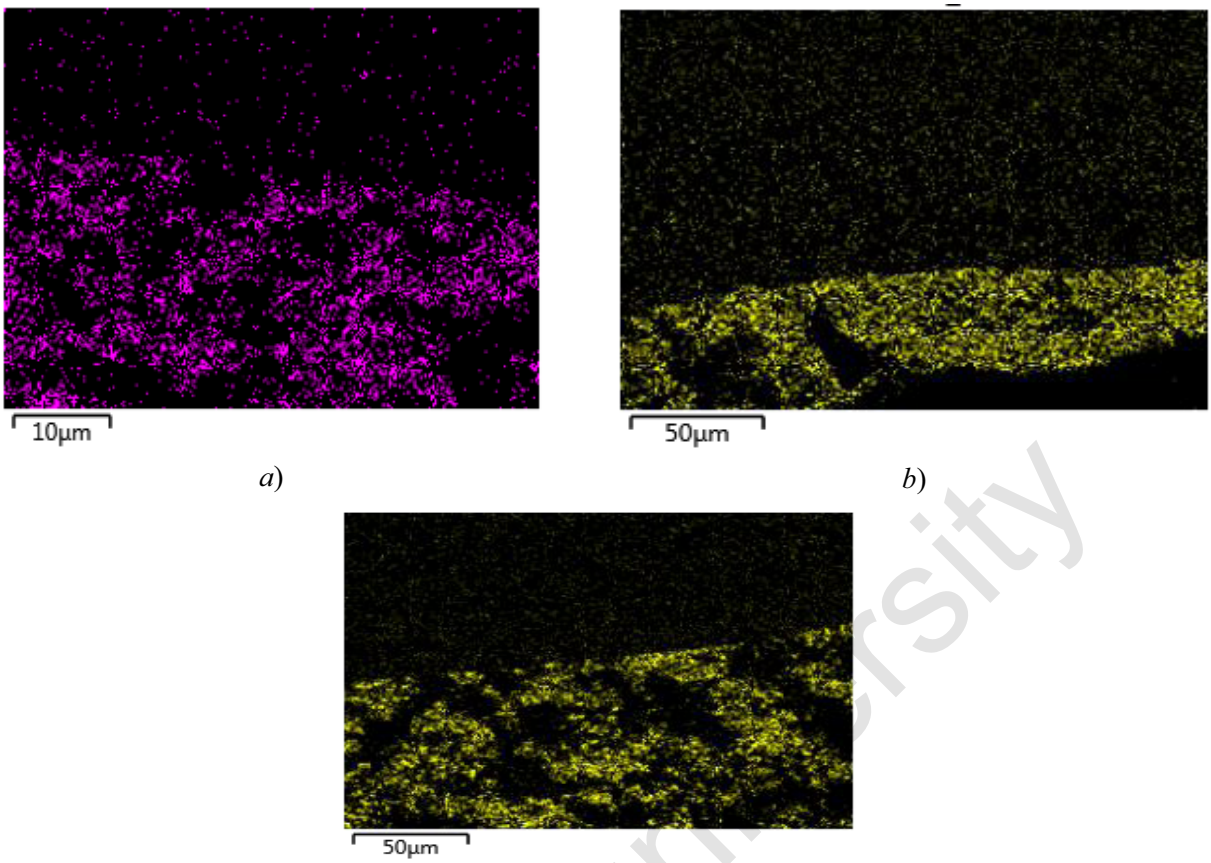

a) *b*) *c*)

Figure 8. EDS analysis of Ni distribution at the electrode–electrolyte interface for different electrode types: (*a*) electrode type—50Ni-n/50ScSZ-n; (*b*) electrode type—40Ni-n/60ScSZ-m; (*c*) electrode type—40Ni-m/60ScSZ-m

The data in Figure 8 reveal that the degree of continuity and uniformity in nickel distribution across the electrode–electrolyte interface varies depending on the morphology and dispersity of the composite constituents. In particular, the sample with the 40Ni-n/60ScSZ-m composition (Fig. 8*b*) demonstrates the most uniform and compact contact with the electrolyte. This is attributed to the synergistic effect of nanostructured nickel and submicron-scale ScSZ, which promotes the development of an extended three-phase boundary. The presence of a high density of triple-phase contact points (Ni–ScSZ–gas) in this configuration facilitates enhanced charge transfer and more efficient initiation of electrochemical reactions.

The 50Ni-n/50ScSZ-n sample (Fig. 8*a*), despite containing nanostructured components in both phases, exhibits a less continuous interfacial contact. This may be attributed to an imbalance in particle size distribution and potential phase overlap during suspension mixing, which could hinder the formation of a well-integrated composite structure.

The composite 40Ni-m/60ScSZ-m (Fig. 8*c*), composed of submicron powders, exhibits the sparsest distribution of nickel at the electrode–electrolyte interface, indicating a lower density of effective active zones. Accordingly, based on the composition and dispersity of the components, a trend can be established in the increasing density of the interfacial contact zone—and, consequently, the concentration of active triple-phase boundaries—as follows: m–m < n–n < n–m. These findings align well with previously obtained polarization resistance data, where samples with more developed interfacial microstructures displayed lower Rη values, thereby confirming the critical role of microstructural architecture in determining anode performance efficiency.

Figure 9 presents the concentration-dependent behavior of the total polarization resistance (Rη) for four different types of Ni/ScSZ-based anodes: Ni-n/ScSZ-n, Ni-n/ScSZ-m, Ni-m/ScSZ-m, and Ni-n/ScSZ-n-film, measured at 800 °C and 900 °C. The analysis of these trends provides insight into the influence of both the

dispersion of the component powders and the method of anode structure formation on the electrochemical performance of the composites.

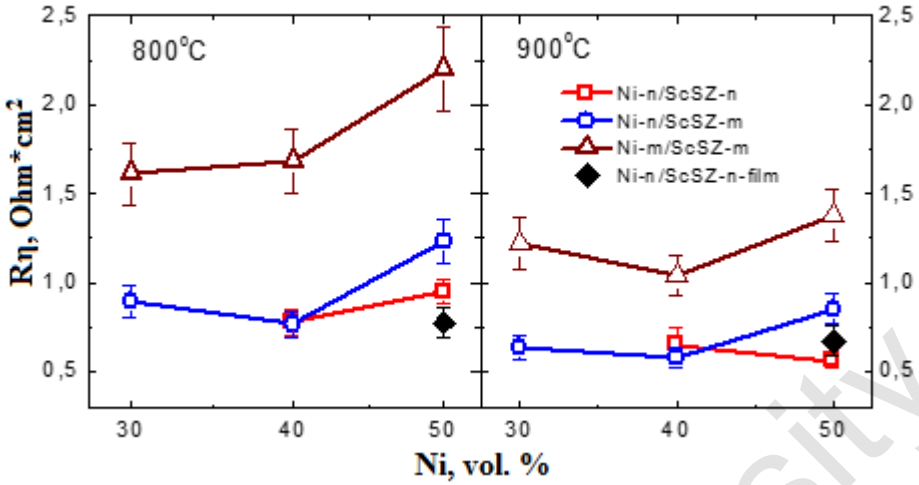

Figure 9. Dependence of the total polarization resistance Rη of three types of composite anodes on Ni content in the composite at 800 and 900 °C

The most significant reduction in polarization resistance is achieved when nanostructured nickel is combined with a submicron electrolyte (Ni-n/ScSZ-m), particularly at a Ni content of approximately 40 vol.%, where a distinct minimum in Rη is observed. This improvement is attributed to the formation of an optimal triple-phase boundary and a more efficient distribution of conductive pathways. A similar minimum is also evident for Ni-m/ScSZ-m anodes; however, their polarization resistance values are higher due to a lower active surface area and a coarser microstructure. These findings are consistent with the results reported in [18], which examined a Ni/YSZ anode prepared via co-precipitation.

The Ni-n/ScSZ-n anode exhibits the lowest polarization resistance at 900 °C (~0.56 Ohm·cm^2), with only a slight increase to ~0.9 Ohm·cm^2 when the temperature is reduced to 800 °C, indicating excellent thermal stability. The Ni-n/50ScSZ-n-film anode, prepared via tape casting and co-sintering, also shows consistently low polarization resistance across the investigated temperature range. At 800 °C, its resistance is approximately 0.85 Ohm·cm^2, decreasing to around 0.75 Ohm·cm^2 at 900 °C, which is characteristic of thermally activated charge transfer processes. Despite its denser structure and lower porosity compared to samples fabricated via screen-printing, the film-based anode maintains high electrochemical performance. This highlights the effectiveness of interface formation during the casting process, as well as the presence of a sufficiently developed triple-phase boundary that supports favorable conditions for electrochemical reactions.

Table 2 summarizes the activation energy (E_a) values for Ni/ScSZ anode composites with varying particle size distributions at nickel volume concentrations of 30 %, 40 %, and 50 %. Analysis of the data reveals a pronounced impact of microstructural parameters on the kinetics of electrode processes. For the Ni-n/ScSZ-n composition—where both components are nanostructured—the activation energy reaches 65.5 ± 5.1 kJ/mol, which is significantly higher compared to the other formulations. This value notably exceeds the typical activation energy associated with surface reactions, suggesting a more complex or energy-intensive charge transfer mechanism in this microstructure.

$$OH_{Ni} + H_{Ni} \rightarrow H_2O_{Ni} + Ni \quad (1)$$

This surface reaction exhibits an activation energy of 42.7 kJ/mol and is likely the dominant contributor to the polarization resistance observed in the electrodes studied in this work. It represents a model anodic electrochemical process in solid oxide fuel cells (SOFCs), describing the surface interaction between adsorbed hydroxyl (OH) and hydrogen (H) species on the nickel surface, leading to the formation of water and the concomitant reduction of nickel. This reaction can be considered a simplified depiction of one of the elementary steps involved in the electrochemical oxidation of hydrogen at the anode.

Table 2

Activation energy of the electrode process

Composite Type Ni / ScSZ	E_a, kJ/mol		
	C_{Ni} = 30 vol.%	C_{Ni} = 40 vol.%	C_{Ni} = 50 vol.%
n/n	–	36.5±9.8	65.5±5.1
n/m	33.3±2.8	43.3±4.9	42.9±4.6
m/m	32.1±4.8	48.9±2.8	44.4±6.8
n/n-film	–	–	40.0±6.0

This increase in the activation energy barrier is likely associated with the specific microstructural features of the composite formed during bulk pressing and sintering. In particular, excessive overlapping of the ScSZ-n nanoparticles—lacking electronic conductivity—may reduce the effectiveness of the interfacial contact between phases, thereby hindering charge transfer across the triple-phase boundaries.

Support for this microstructural influence hypothesis comes from the results obtained for the Ni-n/ScSZ-n-film sample, fabricated using a lamination technique. Despite having an identical chemical composition and particle dispersion, this film-type anode exhibited a significantly lower activation energy of 40.0 ± 6.0 kJ/mol compared to its bulk-pressed counterpart. This observation underscores the critical importance of controlled microstructure formation, which enables more favorable conditions for interfacial interaction and efficient charge transfer between phases.

An analysis of the impedance spectra for cells with 50Ni-n/50ScSZ-n electrodes, based on the data presented in Figure 10, highlights the influence of electrode fabrication techniques on the electrochemical characteristics of the cells.

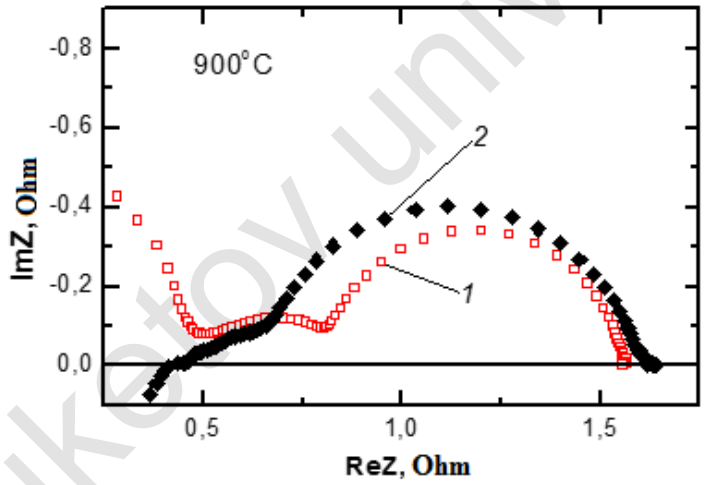

Figure10. Impedance spectra of cells with 50Ni-n/50ScSZ-n electrodes:
(*1*)—cells with electrodes applied by painting; (*2*)—cells with electrodes applied by co-sintering

The spectra allow for a comparison between two types of electrodes prepared by different methods: the first sample (curve 1) was produced using the traditional ink-based painting technique to apply the anode layer, while the second (curve 2) involved co-sintering of pre-formed film laminates.

The impedance spectra shown in Figure 10 provide insight into the effect of electrode fabrication methods on the polarization behavior of the anodes. A comparison of the two samples, represented by curves (1) and (2), reveals that the second electrode (curve 2) exhibits a lower high-frequency component of the polarization resistance ($R_{\eta\text{-HF}}$), indicating more efficient charge transfer at the electrode–electrolyte interface. This reduction in resistance is likely attributed to the formation of a denser and more uniform interface achieved through the co-sintering method, which reduces defects commonly associated with electrodes applied via painting techniques.

At the same time, the low-frequency component ($R_{\eta\text{-LF}}$) shown in Figure 10, which is associated with diffusion processes within the porous anode structure, is higher for the second sample. This is likely due to reduced porosity, which limits the transport of gaseous species. Nevertheless, the total polarization resistance of the anode corresponding to curve (2) remains comparable to or even lower than that of the anode fabricat-

ed by the conventional painting method. These findings highlight the potential of alternative electrode fabrication techniques for enhancing the electrochemical performance of solid oxide fuel cells (SOFCs) [19, 20].

Conclusion

This study presents a comprehensive investigation into the effects of particle size distribution and volume ratio of components in Ni/ScSZ-based cermet composites—comprising nickel and scandia-stabilized zirconia (Sc_2O_3-stabilized ZrO_2)—on their sintering behavior, electrical properties, and electrochemical performance as anodes for solid oxide fuel cells (SOFCs). The composites were synthesized using nano- and submicron-sized powders of NiO and ScSZ (10.5 mol% Sc_2O_3), with particle sizes ranging from 20 to 330 nm. Three types of composites differing in phase dispersity were examined: "nano–nano", "nano–micro", and "micro–micro", with the nickel volume fraction varied between 10 and 50 vol%.

It was established that the percolation threshold, marking the transition from purely ionic to mixed ionic-electronic conductivity, is influenced by the particle size ratio of the composite constituents: for the "nano–nano" system, the threshold occurs at approximately 35 vol% Ni, while in other systems it is reached around 30 vol%. The lowest polarization resistance (\~0.55 Ω·cm² at 900 °C) was observed in anodes containing about 40 vol% nickel, attributed to the optimal development of the triple-phase boundary. The incorporation of nanoscale components—either one or both phases-led to a significant enhancement in the electrochemical performance of the anodes compared to their submicron counterparts.

It was found that the percolation threshold, which governs the transition from ionic to mixed conductivity, strongly depends on the particle size ratio of the composite components. For the "nano–nano" systems, this threshold is reached at approximately 35 vol% Ni, whereas in other types of composites it occurs near 30 vol%. The lowest polarization resistance (\~0.55 Ω·cm² at 900 °C) was observed for anodes containing around 40 vol% Ni, which correlates with the optimal development of the triple-phase boundary. Incorporating nanostructured components—either partially or entirely—led to a marked improvement in the electrochemical performance of the anodes compared to those composed of submicron powders.

These results validate the effectiveness of an integrated strategy for optimizing the morphology and phase composition of Ni/ScSZ-based anodes and highlight the practical potential of such composites for use in high-performance, energy-efficient solid oxide fuel cell technologies.

Acknowledgments

This research has been funded by the Science Committee of the Ministry of Science and Higher Education of the Republic of Kazakhstan (Grant No. AP19680484).

References

1 Vafaeenezhad, S., Hanifi, A.R., Laguna-Bercero, M.A., & Sarkar, P. (2022). Microstructure and long-term stability of Ni–YSZ anode supported fuel cells: A review. *Journal of Power Sources, 541*, 231–244. https://doi.org/10.1016/j.jpowsour.2022.231944.

2 Wang, X., Zhang, Y., Zhang, H., & Han, M. (2024). Mechanism analysis of the reduction process of the NiO–YSZ anode of a solid oxide fuel cell by hydrogen. *Journal of The Electrochemical Society, 171*(9), 091501. https://doi.org/10.1149/1945-7111/ad1649.

3 Rao, M., Sun, X., & Hagen, A. (2020). Durability of solid oxide electrolysis stack under dynamic load cycling for syngas production. *arXiv preprint, arXiv:2002*.02169. https://arxiv.org/abs/2002.02169.

4 Omeiza, L.A., Kabyshev, A., Bekmyrza, K., Kubenova, M., Kuterbekov, K.A., Baratova, A., Adaikhan, S., Bakar, S.A., Azad, A.K. (2024). Strontium-Doped BaZr0.8Ni0.2O3-δ Cobalt-Free Cathode Materials for Solid Oxide Fuel Cell. *International Journal of Precision Engineering and Manufacturing-Green Technology, 12*(4), 1295–1307. https://doi.org/10.1007/s40684-024-00667-z.

5 Drosakis, C., Douvartzides, S., Athanasiou, C., & Skodras, G. (2024). Recent Progress on the Materials of Oxygen Ion-Conducting Solid Oxide Fuel Cells and Experimental Analysis of Biogas-Assisted Electrolysis over a LSC Anode. *Energies, 17*(22), 5526. https://doi.org/10.3390/en17225526.

6 Arifin, N., Afifi, A.A., Samreen, A., Hafriz, R.S., & Muchtar A. (2023). Characteristic and challenges of scandia stabilized zirconia as solid oxide fuel cell material — In depth review. *Solid State Ionics. 399*, 116302. http://dx.doi.org/10.2139/ssrn.4419870.

7 Kuterbekov, K.A., Bekmyrza, K.Zh., Kabyshev, A.M., Kubenova, M.M., Aidarbekov, N.K., & Nurkenov, S.A. (2022). Investigation of the Characteristics of Materials with the Ruddlesden-Popper Structure for Solid Oxide Fuel Cells. *Bulletin of the Karaganda University, Physics Series, 108*(4), 32–47. https://doi.org/10.31489/2022ph4/32-47.

8 Feng, Z., Hansen, K., Bhandari, H.B., & Vohs, J. (2024). Stabilization of Ni-Ysz Anodes Using an Ald-Grown Aluminum Titanate Interlayer. *ECS Advances, 3*(2), 024502.https://ssrn.com/abstract=4625745 or http://dx.doi.org/10.2139/ssrn.4625745.

9 Helal, H., Ahrouch, M., Rabehi, A., Zappa, D., & Comini, E. (2024). Nanostructured Materials for Enhanced Performance of Solid Oxide Fuel Cells: A Comprehensive Review. *Crystals, 14*, 306. https://doi.org/10.3390/cryst14040306.

10 Liang, F., Su, Y., Zhou, P., Pan, Z., Yao, P., Bian, L., Jiao, Z., Yan, Z., Yuan, Q., & Wu, J. (2025). Realizing a Robust High‐Performance Ni‐GDC Nanocomposite Anode for SOFCs by Self‐Assembly of Reactive Cosputtered Nanolayers, *Nano Letters, 25*(11), 4276–4283. https://doi.org/10.1021/acs.nanolett.4c05909.

11 Arifin, N.A., Afifi, A.A., Kumar, N., Roslan, N.N., & Muchtar A. (2024). Influence of Metal Dopant (Cu, Co, Sm, Sn) on Ni/ScSZ Thin Film Anode in Solid Oxide Fuel Cell. *Journal of Regional Development and Technology Initiatives, 2*(2), 103–117. https://doi.org/10.58764/j.jrdti.2024.2.81.

12 Timurkutluk, B., Ari, A., Altan T., & Genc O. (2024). Evaluation of anode support microstructure in solid oxide fuel cells using virtual 3D reconstruction: A simulation study. *International Journal of Hydrogen Energy, 82*, 1157–1170, https://doi.org/10.1016/j.ijhydene.2024.08.066.

13 Nikonov, A.V., Pavzderin, N.B., Khrustov, V.R., Semenova, I.V., Demidova, K.I., Kuterbekov, K.A., Bekmyrza, K.Zh., Nurakov, S.N., Koketay, T.A., & Gyrdasova, O.I. (2021). Investigation of thermal, electrical, and electrochemical properties of $Pr_{1-x}Sr_xFe_{1-y}Co_yO_3$ ($0 < x < 0.4$; $y = 0.2$, 0.5) cathode materials for SOFC. *Journal of Alloys and Compounds, 865*, 158898, https://doi.org/10.1016/j.jallcom.2021.158898.

14 Rakhadilov, B.K., Berdimuratov, N.E., Zhurerova, L.G., Bayatanova, L.B., Kurbanbekov, Sh.R., & Satbayeva, Z.A. (2023). Study of the VAC of the EPCTT process with varying electrode parameters. *Bulletin of the Karaganda University «Physics Series», 111*(3), 13632–142. https://doi.org/10.31489/2023ph3/136-142.

15 Auner, A. W., Burton, M. A., Nagel, L. A., Crowhurst, J. C., Weisz, D.G., & Knight, K. B. (2024). A comparative study of cerium oxides formed by pulsed laser ablation and continuous wave laser heating. *Journal of the American Ceramic Society, 107*(3), 514–521. https://doi.org/10.1111/jace.19429.

16 Prakash, B.S., Kumar, S.S., & Aruna, S.T. (2014). Properties and development of Ni/YSZ as an anode material in solid oxide fuel cell: A review. *Renewable and Sustainable Energy Reviews, 36*, 149–179. https://doi.org/10.1016/j.rser.2014.04.043.

17 Develos-Bagarinao, K., Yamaguchi, T., & Kishimoto, H. (2023). Elucidating the performance benefits enabled by YSZ/Ni–YSZ bilayer thin films in a porous anode-supported cell architecture. *Nanoscale, 15*(27), 11569–11581, https://doi.org/10.1039/D3NR01604H

18 Xi, X., Abe, H., & Naito, M. (2014). Effect of composition on microstructure and polarization resistance of solid oxide fuel cell anode Ni–YSZ composites made by co-precipitation. *Ceramics International, 40*(10), 16549–16555. https://doi.org/10.1016/j.ceramint.2014.08.009.

19 Fernandez Visentini, A., de Anna, P., Jougnot, D., & Lehmann, P. (2023). Electrical Signatures of Diffusion-Limited Mixing: Insights from a Milli-fluidic Tracer Experiment. *Transp Porous Med, 146*, 435–461. https://doi.org/10.1007/s11242-021-01607-0.

20 Asenbauer, J., Eisenmann, T., Kuenzel, M., Kazzazi, A., Chen, Z., & Bresser, D. (2020). The success story of graphite as a lithium-ion anode material — fundamentals, remaining challenges, and recent developments including silicon (oxide) composites. *Sustainable Energy & Fuels, 4*(12), 5387–5416. https://doi.org/10.1039/D0SE00175A.

С. Адайхан, К.Ж. Бекмырза, А.А. Баратова, А.М. Кабышев, П. Раджагопал,
Н.К. Айдарбеков, К.К. Кутербеков, М.М. Кубенова, М.Д. Қуаныш

Қатты оксидты отын элементтері үшін Ni–ScSZ наноқұрылымды композиттің анодтарын әзірлеу және сипаттау

Мақалада никель және скандий оксидімен тұрақтандырылған цирконий диоксидіне (Ni/ScSZ) негізделген анодты композиттер қасиеттерінің жан-жақты зерттелуі ұсынылған. Композиттер әртүрлі дисперстік ұнтақтардан керамикалық технология арқылы дайындалды. Зерттеу барысында компоненттердің морфологиясы мен олардың көлемдік қатынасының қыздырғанда тығыздалу, электрөткізгіштік және поляризациялық кедергіге әсері қарастырылды. Нано-, субмикрон- және микроөлшемді бөлшектері бар үлгілер салыстырмалы түрде зерттеліп, тиімді өткізгіштік тор құрылуын және кедергілерді азайтатын оңтайлы параметрлер анықталды. Дилатометрия, электрлік өлшеулер және импенданстық спектроскопия нәтижелері бойынша, нанодисперстік компоненттерді қолдану біртекті құрылым мен жақсы таратылған кеуектілік қалыптастырып, жылулық тұрақтылық пен электрохимиялық тиімділікті арттырады. Ni/ScSZ негізіндегі материалдар дәстүрлі Ni/YSZ анодтарының орнына қолдануға жарамды, себебі олар жоғары ионөткізгіштікке және деградацияға төзімділікке ие. Бұл оларды жоғары тиімді және ұзақ қызмет ететін ҚООЭ жүйелерін дамытуға болашағы зор етеді.

Кілт сөздер: қатты оксидты отын элементі (ҚООЭ), Ni/YSZ аноды, наноқұрам, поляризациялық кедергі, үш фазалы шекара, электрөткізгіштік, тығыздалу кинетикасы, белсендіру энергиясы, импендастық спектроскопия, дайындалу әдісі

С. Адайхан, К.Ж. Бекмырза, А.А. Баратова, А.М. Кабышев, П. Раджагопал,
Н.К. Айдарбеков, К.К. Кутербеков, М.М. Кубенова, М.Д. Қуаныш

Разработка и характеристика наноструктурированных композитных анодов Ni-ScSZ для твердооксидных топливных элементов

В статье представлено всестороннее исследование анодных композитов на основе никеля и стабилизированного оксида циркония с добавкой оксида скандия (Ni/ScSZ), полученных методом керамической технологии из порошков с различной дисперсностью. Основное внимание уделено влиянию морфологии исходных компонентов и их соотношений на процессы спекания, электрическую проводимость и сопротивление поляризации в условиях работы твердооксидных топливных элементов (ТОТЭ). В ходе исследования сравнивались образцы, содержащие нано-, субмикро- и микрочастицы, с целью определения оптимальных параметров, обеспечивающих формирование эффективной проводящей сети и снижение потерь. Согласно данным дилатометрии, измерений проводимости и импедансной спектроскопии, использование нанокомпонентов способствует образованию однородной и плотной микроструктуры с равномерной пористостью, что обеспечивает высокую термическую стабильность и улучшенные электрохимические характеристики. Установлено, что композиты Ni/ScSZ могут стать перспективной заменой традиционным анодам на основе Ni/YSZ благодаря лучшей ионной проводимости и устойчивости к деградации, что делает их привлекательными для разработки более долговечных и эффективных систем ТОТЭ.

Ключевые слова: твердооксидный топливный элемент (ТОТЭ), анод Ni/ScSZ, нанопорошки, сопротивление поляризации, тройная фазная граница, электрическая проводимость, кинетика спекания, энергия активации, импедансная спектроскопия, метод получения

Information about the authors

Adaikhan, Saule — PhD student, L.N. Gumilyov Eurasian National University, Astana, Kazakhstan; e-mail: adaikhansaule@gmail.com.

Bekmyrza, Kenzhebatyr — PhD, Teacher-Researcher, Associated professor, L.N. Gumilyov Eurasian National University, Astana, Kazakhstan; SCOPUS Author ID: 55227303800; ORCID ID: 0000-0001-8902-8736; e-mail: kbekmyrza@yandex.kz.

Baratova, Aliya (*contact person*) — Candidate of Physical and Mathematical Sciences, Senior Teacher, L.N. Gumilyov Eurasian National University, Astana, Kazakhstan; SCOPUS Author ID 55221822500; ORCID ID: 0000-0002-7015-3657; e-mail: aa.baratova@yandex.kz.

Kabyshev, Asset — PhD, Teacher-Researcher, L.N. Gumilyov Eurasian National University, Astana, Kazakhstan; SCOPUS Author ID: 56177620700; ORCID ID: 0000-0003-1472-4045; e-mail: assetenu@gmail.com.

Rajagopal, Packiaraj — PhD, Postodoc, L.N. Gumilyov Eurasian National University, Astana, Kazakhstan; SCOPUS Author ID: 57202507376; ORCID ID: 0000-0001-6336-9524; e-mail: drpackiaraj93@gmail.com.

Aidarbekov, Nursultan — PhD, Senior Teacher, L.N. Gumilyov Eurasian National University, Astana, Kazakhstan; SCOPUS Author ID: 57222254501; ORCID ID 0000-0002-1981-5416; e-mail: nursultan02_22.10.92@mail.ru.

Kuterbekov, Kairat — Doctor of Physical and Mathematical Sciences, Professor, Teacher-Researcher, L.N. Gumilyov Eurasian National University, Astana, Kazakhstan; SCOPUS Author ID: 6603440057; ORCID ID: 0000-0001-5421-271X; e-mail: kkuterbekov@gmail.com.

Kubenova, Marzhan — PhD, Teacher-Researcher, L.N. Gumilyov Eurasian National University, Astana, Kazakhstan; SCOPUS Author ID 57197744698; ORCID ID: 0000-0002-7015-3657; e-mail: kubenova.m@yandex.kz.

Kuanysh, Maral — Master student, L.N. Gumilyov Eurasian National University, Astana, Kazakhstan; e-mail: markamellyy@mail.ru.